Finite element analysis of strain effects on electronic and transport properties in quantum dots and wires

H. T. Johnson, L. B. Freund, C. D. Akyüz, and A. Zaslavsky
Division of Engineering, Brown University, Providence, Rhode Island 02912

(Received 30 April 1998; accepted for publication 6 July 1998)

Lattice mismatch in epitaxial layered heterostructures with small characteristic lengths induces large, spatially nonuniform strains. The components of the strain tensor have been shown experimentally to affect the electronic properties of semiconductor structures. Here, a technique is presented for calculating the influence of strain on electronic properties. First, the linear elastic strain in a quantum dot or wire is determined by a finite element calculation. A strain-induced potential field that shifts and couples the valence subbands in the structure is then determined from deformation potential theory. The time-independent Schrödinger equation, including the nonuniform strain-induced potential and a potential due to the heterostructure layers, is then solved, also by means of the finite element method. The solution consists of the wave functions and energies of states confined to the active region of the structure; these are the features which govern the electronic and transport properties of devices. As examples, two Si_xGe_{1-x} submicron resonant tunneling devices, a quantum wire with two-dimensional confinement and a quantum dot with three-dimensional confinement, are analyzed. Experimentally measured resonant tunneling current peaks corresponding to the valence subbands in the material are modeled by generating densities of confined states in the structures. Size and composition-dependent strain effects are examined for both devices. In both the quantum dot and the quantum wire, the strain effects on the wave functions and energies of confined states are evident in the calculated densities of confined states in the structures, which are found to be consistent with experimentally measured tunneling current/voltage curves for resonant tunneling diodes. © *1998 American Institute of Physics.*
[S0021-8979(98)06419-6]

I. INTRODUCTION

Epitaxially grown semiconductor heterostructures often consist of materials with lattice parameters that are mismatched by as much as several percent. For thin films of large lateral extent, these strains are spatially uniform and the effects are well understood. However, structures of relatively small lateral extent, having distinctive geometric features and bounded by free surfaces, are characterized by strains that are highly nonuniform. The effects of nonuniform strain on the electronic properties of semiconductor heterostructures have been observed experimentally, but the coupled physical phenomenon has not been extensively modeled.[1–4] The analysis of strain effects in a quantum mechanical model of semiconductor devices has only recently been attempted by Pryor *et al.*,[5–7] Williamson *et al.*,[8] and Grundmann *et al.*,[9] who calculate strain-induced potentials and wave functions in quantum dots, and Zunger,[10] who reviews the topic of electronic structure in pyramidal semiconductor quantum dots based on atomistic methods. Few studies have made contact with experimental measurements; Pistol *et al.*[11] model strain effects on the band gap in buried quantum dots, which is consistent with photoluminescence data.

Strained semiconductor devices that are based on quantum effects, particularly charge confinement in one or more spatial dimensions, underlie a potentially significant technology. Much can be learned about quantum effects by studying the class of devices based on resonant tunneling of carriers from an emitter region, into a quantum well, and then into a collector region. The material combinations in these devices and their geometrical features, including the layered structure and the free surfaces, lead to complicated mechanical strain fields. Because the sequential tunneling of carriers is a simple phenomenon governed by the spectrum of available states in the quantum well, and because the devices are extremely small and the operating temperatures are low, it is likely that the effects of strain on the electronic and transport properties can be represented quantitatively through modeling.

Calculations of elastic strain fields in semiconductor structures are well suited for the finite element method, which is a common tool in continuum mechanics.[2,12] In the technique presented here, the finite element calculation of the strain in a device is made using a general purpose structural mechanics finite element package.[13] However, the use of the finite element method (FEM) in quantum mechanics, which is reviewed by Linderberg,[14] is much less common. Models of semiconductor devices by means of the FEM have been proposed by a number of authors for one- and two-dimensional problems. Several FEM models are available for one-dimensional resonant tunneling structures, which include the effects of arbitrary potential profiles due to layered composition.[15–17] Chen[18] models a one-dimensional resonant tunneling diode using the FEM and calculates a current–voltage curve based on a quantum hydrodynamic model. Electron wave functions and band structures for two-

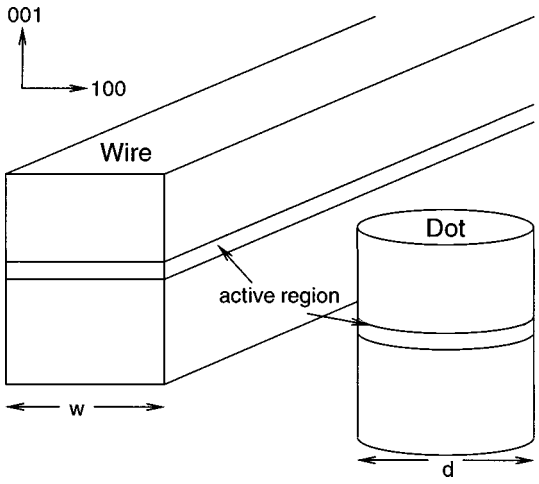

FIG. 1. Schematics of the quantum wire and quantum dot. The row-shaped quantum wire (Ref. 4) has width w and extends a distance much larger than w in the (010) direction. The cylindrical quantum dot (Ref. 2) has diameter d.

dimensional quantum wires or quantum dots are analyzed using FEM by a number of investigators.[19–25] Tsuchida and Tsukada[26] calculate the electronic structure of a perfect Si lattice using a three-dimensional FEM formulation. While some recent models for strain effects have used finite difference methods,[5–9] no three-dimensional FEM quantum mechanical calculations are reported, to the best of our knowledge.

The finite element method is well suited for finding approximate solutions of boundary value problems for partial differential equations in finite domains, especially if the (unknown) exact solution is a minimizer of a total energy functional. Both the stress boundary value problem and the quantum mechanical boundary value problem in the present study are of this type. The central idea of the method is that an unknown continuous field in the domain is represented approximately in terms of its values at discrete points (nodes) within the domain; the goal is to determine optimal values for these nodal quantities. The domain is covered with areas (in two dimensions) or volumes (in three dimensions) whose boundaries are defined geometrically by the nodes; these areas or volumes are the elements. Fields are defined within each element in terms of the values of the nodal quantities on its boundary by means of a suitable interpolation scheme. With the complete field defined in terms of the nodal quantities, the total energy can be expressed in terms of the global vector of nodal quantities. Imposition of the condition that the actual values of the nodal quantities must render the total energy a minimum leads to a system of algebraic equations for these values. The method is ideally suited for numerical analysis by computer. In general, it is convergent as nodal spacing diminishes for elliptic partial differential equations which have unique solutions.[27] It should be noted that the method is of far broader applicability than is implied by these introductory comments.

In this work, a finite element model is used to analyze both the continuum mechanics and the valence-band quantum mechanics of a strained semiconductor device. The

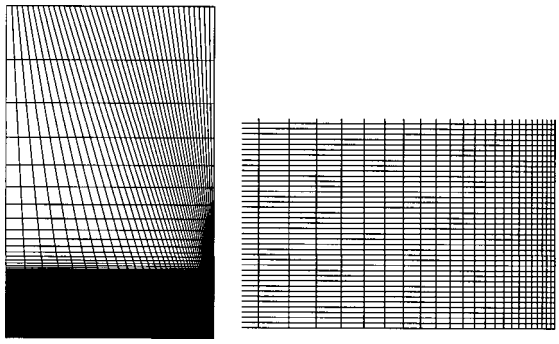

FIG. 2. Finite element mesh used to calculate strain in the quantum wire. Since the strain is symmetric laterally and vertically about the center axes of the device, it is possible to model one quarter of the cross section of the structure only. The mesh for this region, shown on the left, is very highly refined in the active region. A portion of the refined mesh near the edge of the active region is shown on the right.

strain field is shown to affect the performance of the device. The model is used to analyze devices studied experimentally by Akyüz *et al.*[2] and Lukey *et al.*,[4] who show the effects of nonuniform strain on the valence-band resonant tunneling

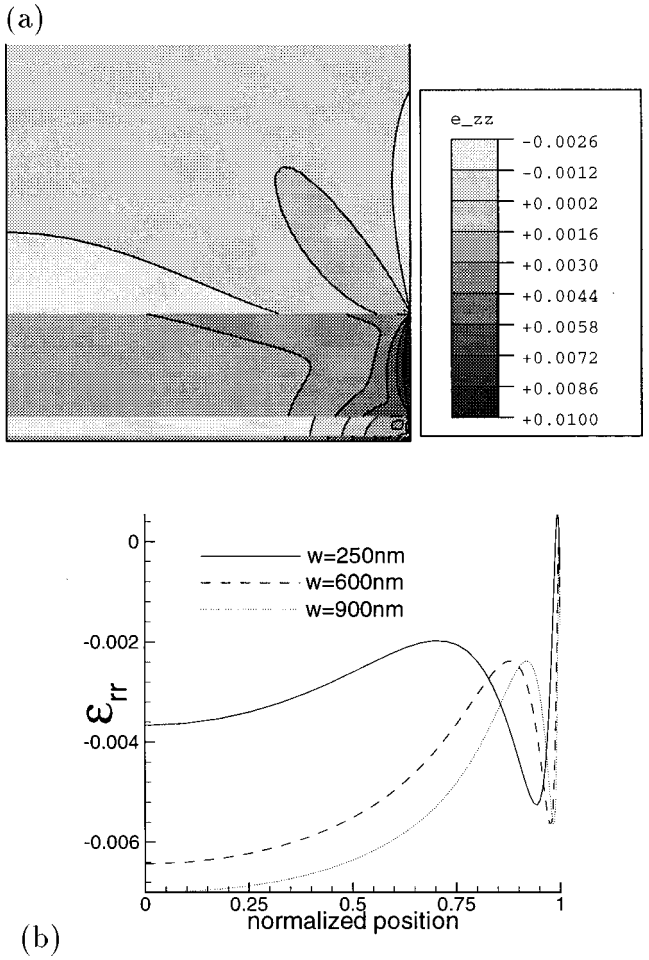

FIG. 3. Measures of strain in the quantum wire. (a) Vertical extensional component of strain (ϵ_{zz}) in the upper half of the quantum wire, from the center to the edge. The bottom two layers are the center of the quantum well layer, and the upper barrier layer. (b) Radial extensional component of strain (ϵ_{rr}) in the center of the well layers of three different wires. The strain is uniform near the center (left), but highly nonuniform near the edge (right).

current versus voltage characteristics of Si_xGe_{1-x} quantum wires and quantum dots, shown schematically in Fig. 1. The main features of the model are described in Sec. II; these include the strain calculation, the treatment of the strain effects by deformation potential theory, and the quantum mechanical model. The finite element formulation for the two- or three-dimensional Schrödinger equation incorporating valence subband coupling and the nonuniform potential is outlined in Sec. III. The results of the calculations for the resonant tunneling structures are discussed in Sec. IV, and comparisons are made between the calculations and the available experimental results.

II. CONTINUUM AND QUANTUM MECHANICAL MODELS

The analysis of a strained semiconductor heterostructure is divided into three calculations. First, a linear elastic finite element calculation is made to determine the strain field, which is a function of the composition and the geometry of the structure. Second, the strain-induced potential field is calculated using deformation potential theory. Third, the time-independent Schrödinger equation including the strain-induced potential is solved numerically by means of the finite element method to obtain the spectrum of energies and wave functions of available states.

A. Strain field calculation

The strain field due to the constraint of epitaxy associated with the mismatched lattice parameters of the heterostructure layers is determined within the framework of linear elasticity theory. The structure is discretized spatially with a mesh, which is more refined near free surfaces and in regions where the mismatch between adjacent layers is larger. The finite element mesh used for a strain calculation in the resonant tunneling diode quantum wire is shown in Fig. 2. The mismatch condition is imposed in the finite element calculation by prescribing in each layer a uniform stress-free dilatation that is proportional to the bulk lattice parameter of the material in that layer. Continuity of displacements is required across the layer interfaces; it is this constraint which gives rise to stress. The outer surfaces are considered to be traction free, implying that certain components of the stress tensor vanish, and the material is allowed to relax until it reaches an equilibrium configuration. Thus, using a standard structural mechanics finite element program,[13] the complete state of stress, strain, and displacement is determined throughout the device. Strain components are shown in Fig. 3 for the resonant tunneling diode quantum wire. Strain is a tensor quantity, and its components show significant variation with position throughout the device. In smaller devices, the strain is more nonuniform due to the pervasive effect of relaxation at the free surfaces.

B. Strain-induced potential

The components of strain induce a potential field that affects the wave functions and energies of the charge carriers in an otherwise perfect crystal. From first-order perturbation theory, the strain-induced potential that affects wave functions in subbands α and β is formed from the tensor product[28]

$$V_{\epsilon}^{\alpha\beta}(\mathbf{r}) = D_{ij}^{\alpha\beta}\epsilon_{ij}(\mathbf{r}), \tag{1}$$

where $\mathbf{r}$ is an arbitrary position vector, $\epsilon_{ij}(\mathbf{r})$ is the strain tensor field, and $D_{ij}^{\alpha\beta}$ is the deformation potential tensor for subbands α and β, which consists of components derived experimentally. The indices ij range over the coordinate directions. For the Si_xGe_{1-x} material combination, the valence-band electronic properties are dominated by the heavy-hole and light-hole subbands, so the $\alpha\beta$ basis includes the heavy-hole (HH) subbands denoted by $|3/2,\pm 3/2\rangle$, and the light-hole (LH) subbands denoted by $|3/2,\pm 1/2\rangle$. The split-off subbands (SO) are ignored because the separation energy is considered to be large enough so that coupling effects can be neglected. The potential equation can be written as

$$V_{\epsilon}^{\alpha\beta}(\mathbf{r}) = \begin{array}{c} \\ |\frac{3}{2},+\frac{3}{2}\rangle \\ |\frac{3}{2},-\frac{3}{2}\rangle \\ |\frac{3}{2},+\frac{1}{2}\rangle \\ |\frac{3}{2},-\frac{1}{2}\rangle \end{array} \begin{array}{c} \begin{array}{cccc} |\frac{3}{2},+\frac{3}{2}\rangle & |\frac{3}{2},-\frac{3}{2}\rangle & |\frac{3}{2},+\frac{1}{2}\rangle & |\frac{3}{2},-\frac{1}{2}\rangle \end{array} \\ \begin{pmatrix} D_{ij}^{11}(\mathbf{r})\epsilon_{ij}(\mathbf{r}) & D_{ij}^{12}(\mathbf{r})\epsilon_{ij}(\mathbf{r}) & D_{ij}^{13}(\mathbf{r})\epsilon_{ij}(\mathbf{r}) & D_{ij}^{14}(\mathbf{r})\epsilon_{ij}(\mathbf{r}) \\ D_{ij}^{21}(\mathbf{r})\epsilon_{ij}(\mathbf{r}) & D_{ij}^{22}(\mathbf{r})\epsilon_{ij}(\mathbf{r}) & D_{ij}^{23}(\mathbf{r})\epsilon_{ij}(\mathbf{r}) & D_{ij}^{24}(\mathbf{r})\epsilon_{ij}(\mathbf{r}) \\ D_{ij}^{31}(\mathbf{r})\epsilon_{ij}(\mathbf{r}) & D_{ij}^{32}(\mathbf{r})\epsilon_{ij}(\mathbf{r}) & D_{ij}^{33}(\mathbf{r})\epsilon_{ij}(\mathbf{r}) & D_{ij}^{34}(\mathbf{r})\epsilon_{ij}(\mathbf{r}) \\ D_{ij}^{41}(\mathbf{r})\epsilon_{ij}(\mathbf{r}) & D_{ij}^{42}(\mathbf{r})\epsilon_{ij}(\mathbf{r}) & D_{ij}^{43}(\mathbf{r})\epsilon_{ij}(\mathbf{r}) & D_{ij}^{44}(\mathbf{r})\epsilon_{ij}(\mathbf{r}) \end{pmatrix} \end{array}, \tag{2}$$

where the terms $D_{ij}^{\alpha\beta}$ are the deformation potential tensors which range over the spatial dimensions i and j. The deformation potential tensors contain material constants, which vary spatially as the composition varies in the device; values of these constants for a wide range of materials are known from experiments. The repeated ij indices indicate the scalar product (contraction over the product of second rank tensors) between the deformation potential tensor and the strain tensor. Details of the $D_{ij}^{\alpha\beta}$ terms are given in Appendix A, along with the material constants used in the calculations. Thus, for a calculated strain tensor function of position $\epsilon_{ij}(\mathbf{r})$, it is possible to calculate the deformation potential function of position $V_{\epsilon}^{\alpha\beta}(\mathbf{r})$ to be included in the quantum mechanical analysis.

C. Quantum mechanical model

In resonant tunneling structures, tunneling currents are determined by available quantized states for individual charge carriers. The energies and wave functions of a single carrier in the semiconductor structure are solutions of the time-independent Schrödinger equation

$$H_{k\cdot p}^{\alpha\beta}(\mathbf{r})\Psi^{\beta}(\mathbf{r})+V^{\alpha\beta}(\mathbf{r})\Psi^{\beta}(\mathbf{r})=E\Psi^{\alpha}(\mathbf{r}), \tag{3}$$

where $\Psi^{\alpha}(\mathbf{r})$ is the wave function in subband α, E is the energy, $H_{k\cdot p}^{\alpha\beta}(\mathbf{r})$ is the $\mathbf{k}\cdot\mathbf{p}$ Hamiltonian operator, and $V^{\alpha\beta}(\mathbf{r})$ is a potential function of position.

The $\mathbf{k}\cdot\mathbf{p}$ perturbation method is used to model the medium. Using this technique, there is a tensor function for the effective mass associated with each subband, and there are $\mathbf{k}\cdot\mathbf{p}$ terms coupling the effective masses in different subbands. Written in the same form as Eq. (2) the Hamiltonian is

$$H_{k\cdot p}^{\alpha\beta}(\mathbf{r})=\begin{array}{c} \\ |\frac{3}{2},+\frac{3}{2}\rangle \\ |\frac{3}{2},-\frac{3}{2}\rangle \\ |\frac{3}{2},+\frac{1}{2}\rangle \\ |\frac{3}{2},-\frac{1}{2}\rangle \end{array}\begin{array}{c} \begin{array}{cccc} |\frac{3}{2},+\frac{3}{2}\rangle & |\frac{3}{2},-\frac{3}{2}\rangle & |\frac{3}{2},+\frac{1}{2}\rangle & |\frac{3}{2},-\frac{1}{2}\rangle \end{array} \\ \begin{pmatrix} L_{ij}^{11}(\mathbf{r})\nabla_{ij}^2 & L_{ij}^{12}(\mathbf{r})\nabla_{ij}^2 & L_{ij}^{13}(\mathbf{r})\nabla_{ij}^2 & L_{ij}^{14}(\mathbf{r})\nabla_{ij}^2 \\ L_{ij}^{21}(\mathbf{r})\nabla_{ij}^2 & L_{ij}^{22}(\mathbf{r})\nabla_{ij}^2 & L_{ij}^{23}(\mathbf{r})\nabla_{ij}^2 & L_{ij}^{24}(\mathbf{r})\nabla_{ij}^2 \\ L_{ij}^{31}(\mathbf{r})\nabla_{ij}^2 & L_{ij}^{32}(\mathbf{r})\nabla_{ij}^2 & L_{ij}^{33}(\mathbf{r})\nabla_{ij}^2 & L_{ij}^{34}(\mathbf{r})\nabla_{ij}^2 \\ L_{ij}^{41}(\mathbf{r})\nabla_{ij}^2 & L_{ij}^{42}(\mathbf{r})\nabla_{ij}^2 & L_{ij}^{43}(\mathbf{r})\nabla_{ij}^2 & L_{ij}^{44}(\mathbf{r})\nabla_{ij}^2 \end{pmatrix} \end{array}, \tag{4}$$

where the $L_{ij}^{\alpha\beta}$ tensors on the diagonal of the matrix are the effective-mass tensors for each subband, and the off-diagonal $L_{ij}^{\alpha\beta}$ tensors introduce a $\mathbf{k}\cdot\mathbf{p}$ coupling of subbands. Like the terms in the deformation potential tensors, the components of $L_{ij}^{\alpha\beta}$ contain material constants, and thus, vary spatially throughout the device. The exact forms of the $L_{ij}^{\alpha\beta}$ tensors, which come from the Luttinger–Kohn Hamiltonian, are given in Appendix A.

The deformation potential and effective-mass material constants in Eqs. (2) and (4) are functions of the local composition of the device. Values for the constants in each layer are given by linear interpolation of the material constants associated with each of the pure elements composing that layer.

The nonuniform potential $V^{\alpha\beta}(\mathbf{r})$ consists of contributions from two sources and is given by

$$V^{\alpha\beta}(\mathbf{r})=V_c^{\alpha\beta}(\mathbf{r})+V_{\epsilon}^{\alpha\beta}(\mathbf{r}), \tag{5}$$

where $V_c^{\alpha\beta}(\mathbf{r})$ is due to the valence-band alignment of material at a given position in the device, and $V_{\epsilon}^{\alpha\beta}(\mathbf{r})$ is the strain-induced potential given in Eq. (1). The strain-induced potential $V_{\epsilon}^{\alpha\beta}(\mathbf{r})$, like the components of the strain tensor, is in general nonuniform in both the lateral directions and the vertical direction in the structure. The composition-based band offset potential $V_c^{\alpha\beta}(\mathbf{r})$ is nonuniform only in the growth, or vertical direction in the structure. The total potential $V^{\alpha\beta}(\mathbf{r})$ is shown in Fig. 4 for a representative quantum dot calculation.

III. FINITE ELEMENT TECHNIQUE FOR THE SCHRÖDINGER EQUATION

A. Finite element formulation

The physical domain of the device is discretized into a mesh of nodes and elements. Elements used for the quantum wires and quantum dots are described in Appendix B. The mesh extends to the free or insulated surfaces, which impose an infinite potential on the wave function. The wave functions and energies of the states localized in the active region are insensitive to remote boundary conditions, i.e., conditions at boundaries located a large distance away relative to the active region size. The mesh is more refined in the active region of the device, where large wave-function gradients are expected.

The form of the Schrödinger equation to be solved on the finite element mesh is obtained by minimizing the total variation of the weak, or Galerkin form of the equation with respect to the wave function. The minimum in variation with respect to the wave function corresponds physically to a minimum energy. Details of the complete variational formulation of the finite element technique used here are included in Appendix B; a general discussion of the variational formulation of the finite element method is given by Strang and Fix.[27] The functional corresponding to the weak form of the time-independent Schrödinger equation with a nonuniform potential (3) is given by

$$\Pi(\Psi^{\alpha})=\int_R \nabla\Psi^{\alpha}L^{\alpha\beta}\nabla\Psi^{\beta}dR + \int_R \Psi^{\alpha}V^{\alpha\beta}\Psi^{\beta}dR-E\int_R \Psi^{\alpha}\Psi^{\beta}dR, \tag{6}$$

where Ψ^{α}, $L^{\alpha\beta}$, and $V^{\alpha\beta}$ are functions of position in the structure. The term $L^{\alpha\beta}$ is taken to be constant within each element of the mesh. The fields Ψ^{α}, $\nabla\Psi^{\alpha}$, and $V^{\alpha\beta}$ are represented by their nodal values. Values throughout each element are determined by interpolation according to the particular shape functions that are adopted. Thus, for shape functions $N(\mathbf{r})$ used here, which are described in more detail in Appendix B, these fields are written as

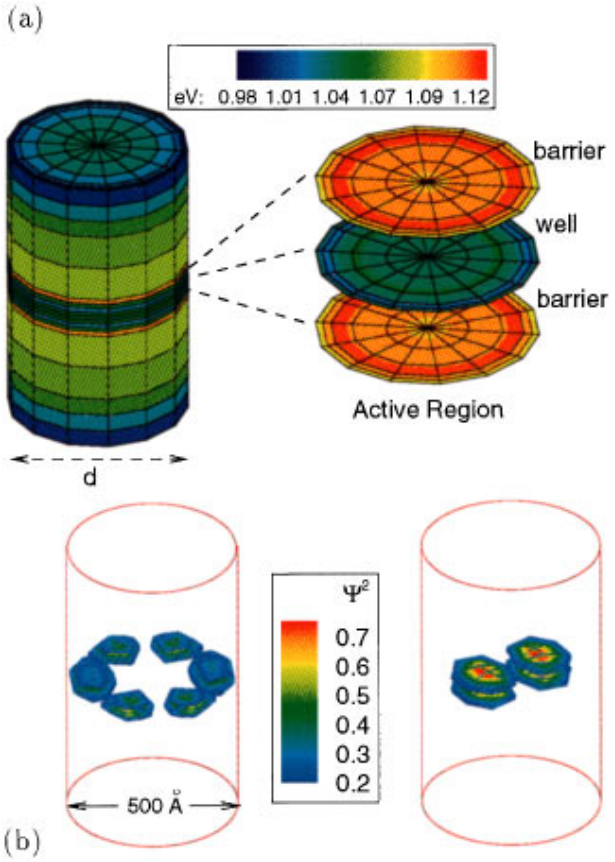

FIG. 4. The potential field for the heavy-hole band in the strained quantum dot, and corresponding representative eigenstates. (a) The axisymmetric potential field is high in the barrier layers and low in the well layer, and radially nonuniform throughout the device. (b) The lower-energy representative eigenstate shown on the left has sixfold angular quantization and is localized in a ring-like region near the outer edge of the device. The higher-energy representative state is confined to the center of the device, with twofold quantization in the angular and vertical directions.

$$\Psi^{\alpha}=\sum_{A=1}^{\text{all nodes}}\Psi_A^{\alpha}N_A(\mathbf{r}),$$
$$\nabla\Psi^{\alpha}=\sum_{B=1}^{\text{all nodes}}\Psi_B^{\alpha}\nabla N_B(\mathbf{r}),\quad V^{\alpha\beta}=\sum_{C=1}^{\text{all nodes}}V_C^{\alpha\beta}N_C(\mathbf{r}), \tag{7}$$

where the coefficients in the summations are the values of the fields at the individual nodes. The functional $\Pi(\Psi^{\alpha})$ is rewritten in a discrete form using Eqs. (7) and then minimized with respect to the nodal values of the wave function, Ψ_A^{α}. Integrals over the region R of the entire structure are replaced with integrals over individual element volumes (Ω^e) and a summation over all elements, so that the finite element form of the Schrödinger equation becomes

$$\sum^{\text{elems}}\left[\sum_A\sum_B\int_{\Omega^e}\left(\nabla N_A L^{\alpha\beta}\nabla N_B+N_AN_B\sum_C V_C^{\alpha\beta}N_C\right)d\Omega\right]$$
$$\times\Psi_B^{\beta}=E\sum^{\text{elems}}\left[\sum_A\sum_B\int_{\Omega^e}N_AN_B\,d\Omega\right]\Psi_B^{\alpha}, \tag{8}$$

which is a form ideally suited for computation.

This form of the Schrödinger equation can be much more simply expressed as

$$K_{ij}\Psi_j=EM_{ij}\Psi_j, \tag{9}$$

where the indices i and j range over all nodal wave-function degrees of freedom, and the repeated indices indicate a summation. Details of the assembly of the matrices K and M are given in Appendix B.

B. Finite element solution

1. Energies and wave functions

The finite element expression of the Schrödinger equation (9) is in the form of a generalized eigenvalue equation. The problem has $n\alpha$ solutions, where n is the total number of nodes in the mesh and α is the number of subbands in the quantum mechanical basis. The solutions consist of energies E and wave functions Ψ. The mesh size used in the calculations reported here results in a very accurate determination of the energies E and good spatial resolution of the wave-functions Ψ, particularly for the lower-energy states. Convergence of the method is found by comparing solutions for meshes with successively decreasing nodal separation. Element refinement is particularly important in the active region of the device, where the wave-function gradients are largest.

Of the $n\alpha$ eigenstates, some states can be found for which the wave function $\Psi(\mathbf{r})$ or the probability density $|\Psi(\mathbf{r})|^2$ is confined to the active region of the device. Examples of eigenstates confined to the quantum well layers of the quantum dot are shown in Fig. 4. The lowest-energy states of these confined eigenstates are the most relevant to transport. For the example of the resonant tunneling diode, sequential tunneling through the double barriers is possible only when the tunneling carriers have energies equal to the energies of the confined states in the quantum well. Thus, over a range of applied biases, the excited carriers can access the confined states and induce a tunneling current only at certain resonances corresponding to the spectrum of eigenvalues given by the finite element solution.

The energy and wave-function solutions reflect the effects of strain, composition, and effective mass on the carriers. The valence-band offset in adjacent layers imposes a large relative potential on the charge carriers, which results in confinement to the quantum well region of the device. The strain-induced potential is considerably smaller than the valence-band potential, but it also shifts the wave functions spatially and energetically. Confined states corresponding to valence subbands with higher effective masses occur at lower energies.

2. Density of states

The density, with respect to energy, of states confined to the active region of the device can be obtained directly from the spectrum of eigenstates given in the finite element solution. This density of confined states is a real-space measure of the electronic properties of the device. Effects due to strain, composition, size, and device characteristics can be seen in the density of confined states. For the example of the resonant tunneling diode, the density of confined states can

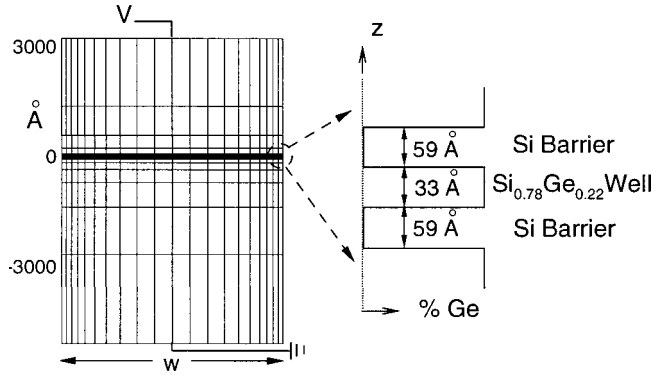

FIG. 5. Schematic of the quantum wire geometry and composition in the active region. The 59 Å Si barriers surround the 33 Å $Si_{0.78}Ge_{0.22}$ quantum well layer. An applied bias V induces a tunneling current in the z direction.

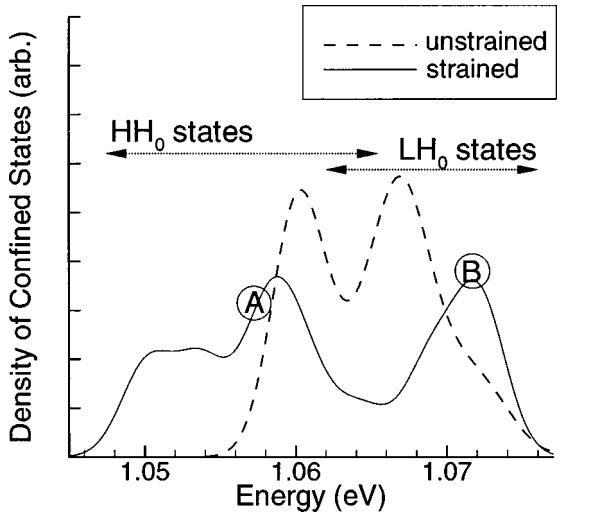

FIG. 6. Density of confined states in the strained quantum wire of width 250 nm. The two large peaks in the dashed curve show the calculated heavy-hole and light-hole resonances without considering strain effects. Strain causes the resonances to separate in energy and induces fine structure in the density of confined states. States at points A (edge state) and B (light-hole state) are shown in Fig. 7.

be used to examine strain effects on the resonant tunneling spectrum. A larger density of confined states with a given energy increases the probability of resonant tunneling by carriers with the same energy. A high probability of tunneling at a given energy is measured experimentally as a tunneling current peak. Thus, the density of confined states can be used to make contact with experimental data.

A Gaussian broadening technique can be used to calculate a continuous density of confined states function $\rho(E)$. The energy E_i of each confined state is broadened by a narrow, normalized Gaussian distribution, and a summation over all n states gives $\rho(E)$ as

$$\rho(E)=\sum_{i=1}^{n} \frac{1}{2a\sqrt{\pi}} \exp(-(E-E_i)^2/4a^2), \tag{10}$$

where a is a free parameter that controls the width of the Gaussian distributions, and thus, the smoothness of the density of states $\rho(E)$. The parameter a is chosen to bring out the general features of $\rho(E)$; the broadening of each state is larger than the typical separation of individual eigenstates, but narrow enough to bring out features of the density of states that are due to small groups of related eigenstates. Typical values of a are on the order of 1 meV.

IV. RESULTS AND COMPARISON TO EXPERIMENTS

A. The Quantum wire

1. Physical system

The quantum wire considered here is a long, row-shaped, layered structure of fixed total height h. The geometry of the structure and the thickness and composition of each layer, based on the experimental work of Lukey *et al.*,[4] are shown in Fig. 5. The middle layers of the device are considered to be the active region, and include the quantum well layer ($Si_{0.78}Ge_{0.22}$) and the two undoped barrier layers (Si). Surrounding the active region are strained ($Si_{0.78}Ge_{0.22}$) emitter and collector regions; the thick outermost layers of the device are Si. A range of widths ω are considered in order to model size-dependent strain effects and to compare results with experimental data.

The device operates by the sequential tunneling of charge carriers from the doped region above the barrier layer, into the quantum well layer, and then through the lower barrier layer. Resonant tunneling spectroscopy is done experimentally by applying a bias across the device and measuring the current of tunneling carriers that is induced. A resonant tunneling spectrum can be compiled by measuring the induced currents associated with a range of applied biases. The experimental result is a resonant tunneling $I(V)$ curve.

2. Strain field

The strain and displacement fields for this geometry are two-dimensional since the constraining effect of the material in the direction along the long axis of the wire imposes a state of plane strain. The mesh is more refined in the active region of the structure and near the traction free lateral surfaces, where the deformation is expected to be more nonuniform. The ϵ_{zz} component of strain (extensional strain in the vertical direction) is shown in Fig. 3 in and near the active region of the device. Figure 3 also shows the ϵ_{rr} component of strain along the centerline of the quantum well layer for structures with three different widths. The important features are that the strain is a tensor valued function and that the relaxing effect of the free surface and the multilayered composition of the structure lead to nonuniform strain components.

3. Results of the quantum mechanical calculation

Solution of the quantum mechanical problem gives the energies and wave functions of states confined to the quantum well layer in the wire. From this spectrum of states, a density of confined states is calculated. The density of confined states for a narrow wire ($w=250$ nm) is shown in Fig. 6, representative eigenstates are shown in Fig. 7, and the

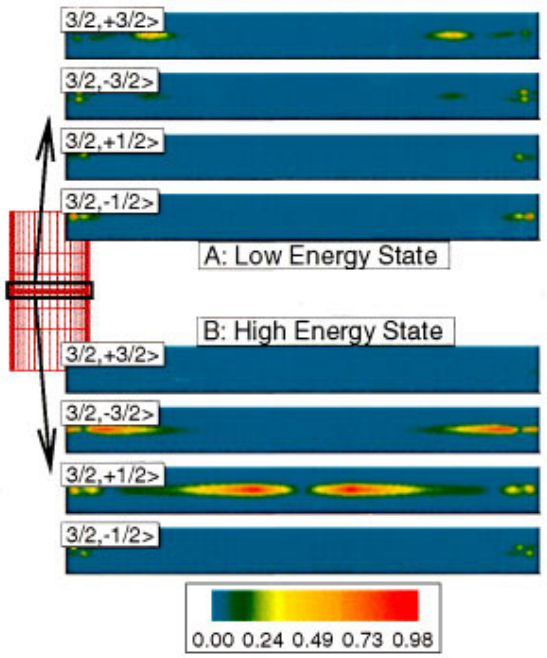

FIG. 7. Probability densities for two representative confined states with energies denoted by A and B in Fig. 6. The four cross sections above show the probability density associated with each of the four valence subbands for a low-energy confined state. The wave function is of mixed type, and localized near the edges of the structure due to strain relaxation. The four lower cross sections show a higher-energy state that is predominantly $|3/2,+1/2\rangle$ type. There is strong mixing with the $|3/2,-3/2\rangle$ subband and there are edge effects due to the relaxed free surfaces.

density of confined states for wide and narrow wires are compared in Fig. 8.

The results of the calculations are consistent with some experimental observations of Lukey *et al.* First, the strain separates the resonant current peaks associated with the heavy-hole and light-hole subbands, as shown in Fig. 6. The

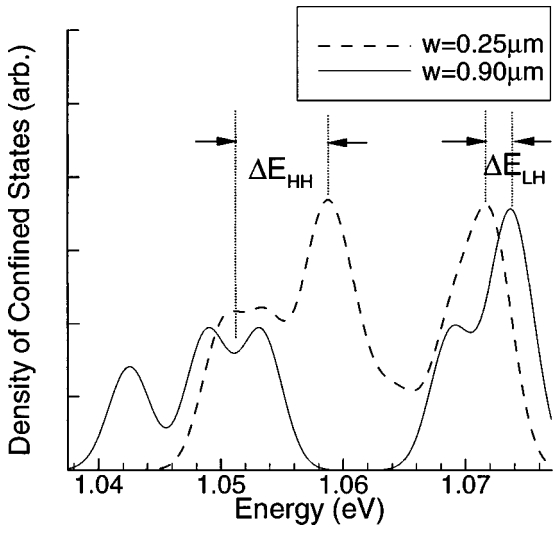

FIG. 8. Densities of confined states for two quantum wires of different widths. The higher average strain in the wider device results in a larger energy separation between heavy-hole and light-hole resonance peaks. The heavy-hole peak is shown to be shifted by the strain more than the light-hole peak.

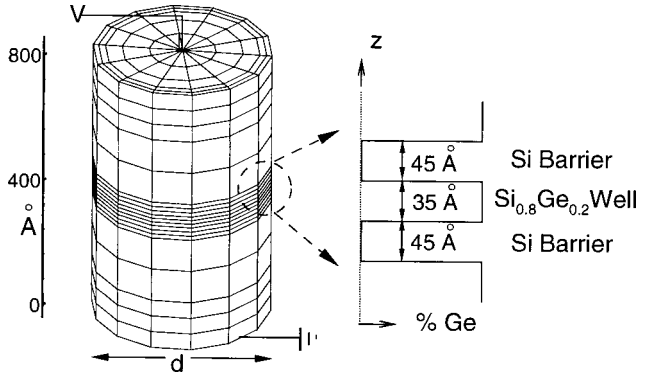

FIG. 9. Geometry and composition of the quantum dot device (Ref. 2). The 45 Å Si barriers surround the 35 Å $Si_{0.75}Ge_{0.25}$ well. The total height is 80 nm, and the diameter d varies. An applied bias V induces a tunneling current in the z direction.

calculation gives a peak separation of about 20 meV, which would correspond to a bias shift of roughly 50 mV. The experimentally measured separation is approximately 90 mV. However, it is important to note that the calculation shown is for a wire aligned along a (100) crystalline axis. The experiments of Lukey *et al.* measured wires aligned along a (110) axis, which would exhibit more sensitivity to strain in the electronic properties due to the form of the deformation potential tensor $D_{ij}^{\alpha\beta}$, and thus, presumably a wider strain-induced peak separation. The second characteristic evident in Fig. 6 is the presence of additional fine features in the density of states. Fine structure is also observed experimentally in the $w=250$ nm device. An examination of the states present over a range of energies shows that the fine features in the density of states are due to groups of similar states separated in energy by the influence of nonuniform strain, as shown in Fig. 7.

The size dependence of the strain effect is demonstrated in the densities of confined states for wires with widths of 250 and 900 nm in Fig. 8. The main feature is the increase in the energy separation of the heavy-hole and light-hole peaks as the wire width increases. This is due to the reduced effect of free-surface strain relaxation in larger devices, where the average strain values approach the bulk film mismatch strains. In the smallest devices, the strain is relaxed over a significant portion of the volume, so the average strain is smaller and the energy separation between the heavy-hole and light-hole peaks is smaller.

B. The quantum dot

1. Physical system

The quantum dot considered here is cylindrical in shape and of fixed height. The features of this structure are based on the experimental work of Zaslavsky *et al.*[1] and Akyüz *et al.*[2] and are shown in Fig. 9 for a representative calculation. The three middle layers, which consist of the quantum well ($Si_{0.75}Ge_{0.25}$) and the barriers (Si), make up the active region of the device. Surrounding the active region are the emitter and collector regions ($Si_{0.75}Ge_{0.25}$), which have rela-

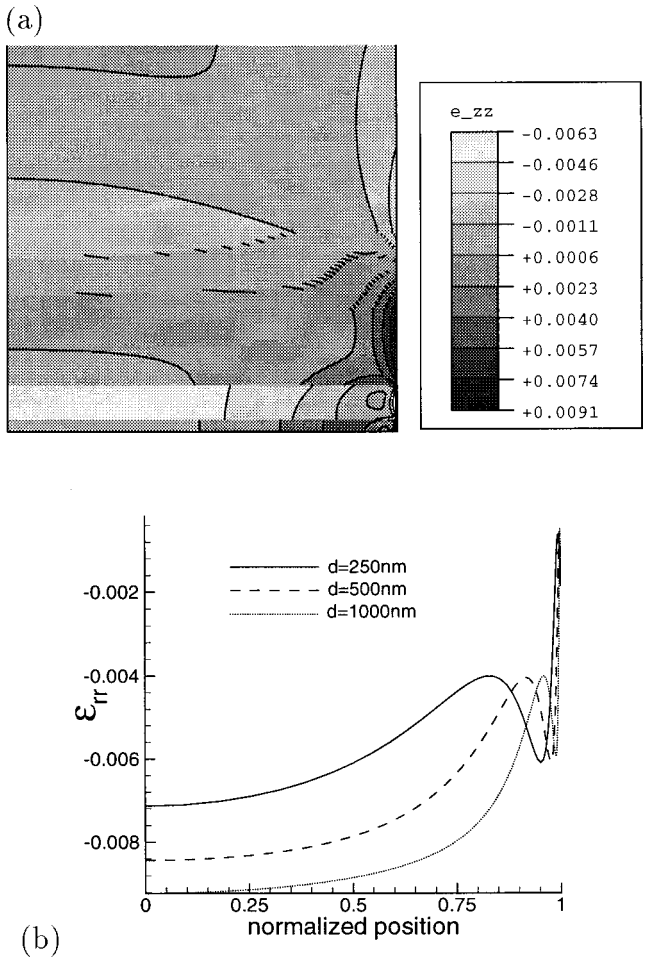

FIG. 10. Measures of strain in the quantum dot. (a) Vertical extensional component of strain (ϵ_{zz}) in the upper half of the quantum dot, from the center to the edge. The bottom two layers are the center of the quantum well layer, and the upper barrier layer. (b) Radial extensional component of strain (ϵ_{rr}) in the center of the well layers of three different dots. The strain is uniform near the center (left), but highly nonuniform near the edge (right).

tively low strain due to the outermost layers which are graded in composition. A range of cylinder diameters d is considered.

The quantum dot device operates on the same resonant tunneling principle as the quantum wire. Carriers tunnel sequentially from the emitter region, through the upper barrier into states in the quantum well, and then through the lower barrier into the collector region. The experimental $I(V)$ curve is a measure of the resonant tunneling spectrum.

2. Strain field

The stress, strain, and displacement fields are axisymmetric for this geometry. The mesh used to calculate the strain extends from the center axis of the structure outward, with increasing refinement near the outer, traction-free surface of the device, where the fields are expected to be more nonuniform. Figure 10 shows the ϵ_{zz} component of strain (extensional strain in the axial direction), and ϵ_{rr}, the extensional strain along a radial line in the midplane of the quantum well, for three different dot diameters. As in the case of

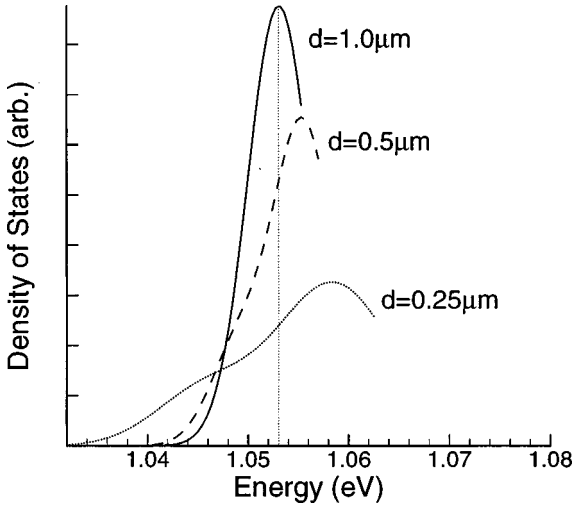

FIG. 11. Densities of heavy-hole confined states for a range of quantum dot diameters. The variation in average strain levels results in the shifting of the peaks for dots of different sizes. The energy shift corresponds to the bias shift measured by Zaslavsky *et al.* (Ref. 1).

the quantum wire, the strain is very nonuniform, and the extent of the nonuniformity increases in smaller structures. This is due to the more significant effect of free-surface proximity.

3. Results of the quantum mechanical calculation

For the three-dimensional quantum dot, a reduced quantum mechanical basis is adopted in order to limit the total number of degrees of freedom in the calculation. To model only the lowest-energy heavy-hole states, it is sufficient to consider a one-dimensional quantum mechanical basis where only the $|3/2,+3/2\rangle$ band is examined, but it is still possible to consider an anisotropic effective mass.

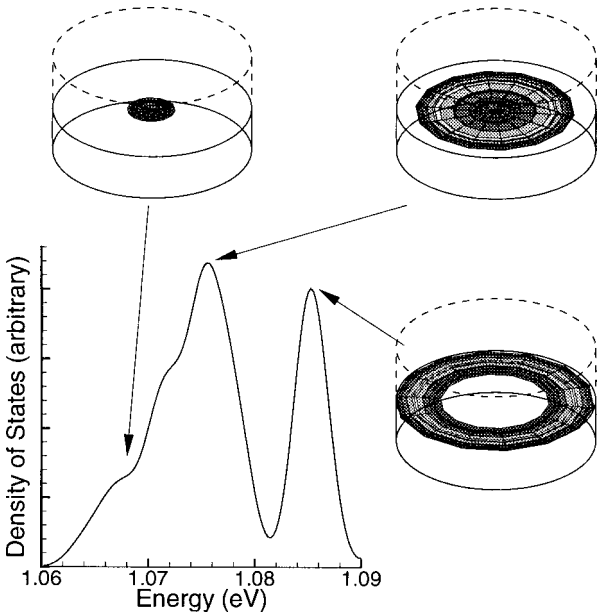

FIG. 12. The effect of strain-induced lateral confinement on the density of confined states. The features of the density of confined states are due to groups of eigenstates with similar lateral quantization.

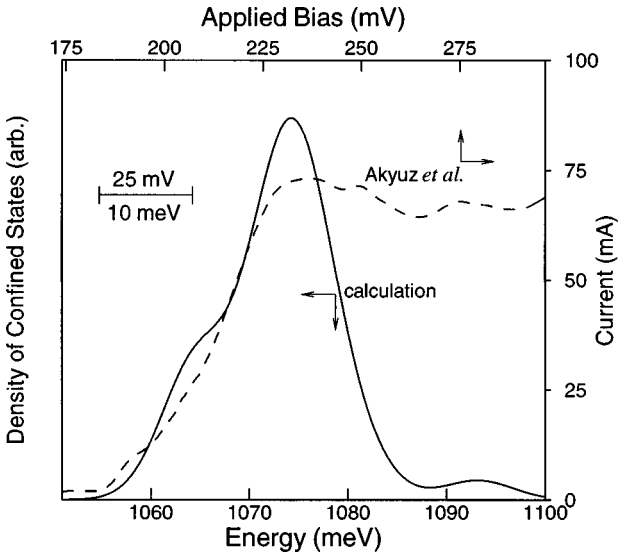

FIG. 13. Fine structure in the density of confined states in the $d=250$ nm quantum dot (Ref. 2). The calculated density of confined states is consistent with the experimental current–voltage curve. The density of confined states calculation does not account for the roughly linear background current that is observed experimentally.

Two significant results compare favorably to the experiments of Zaslavksy *et al.*[1] and Akyüz *et al.*[2] First, as seen in Fig. 11, there is a size dependence of the strain effect on the resonant energies that is similar to the effect in the quantum wires. In larger diameter devices, the average strain is higher because free-surface relaxation is less significant, so the peak is shifted further from an idealized case without strain.

Second, in the smallest devices, there are additional fine features in the density of states that are shown in Fig. 12 to be the result of the influence of nonuniform strain. In agreement with the suggestion of Akyüz *et al.*,[2] it is evident that the relaxed strain near the lateral surface leads to low-energy ring-like heavy-hole states. The strain-induced energy shifting of groups of states produces features in the density of confined states that are consistent with the $I(V)$ curves for devices of the same size. Figure 13 shows a calculated density of confined states plot and a measured $I(V)$ curve for a $d=250$ nm quantum dot with 10 meV on the energy axis equal to 25 mV on the bias axis. Many of the features of the $I(V)$ curve are predicted qualitatively in the density of confined states curve, including fine structure below and above the main heavy-hole resonance energy. However, the density of confined states is not equivalent to the resonant tunneling current; the calculation does not consider some important physical effects, most notably the roughly linear background current in the $I(V)$ relationship.

V. CONCLUSIONS

A finite element technique is presented here which allows for the calculation of strain effects on the electronic and transport properties of strained quantum wires and dots. The approach is similar to some recent work as it is based on a simplified quantum mechanical model,[5–9] but the flexibility of meshing and the low computational cost of the finite element method offer easy access to results which can be compared to experimental data.

The technique is used to examine mismatch strain effects in quantum wires and quantum dots that operate on a simple single carrier sequential tunneling effect. Strain effects are shown to explain several reported trends in experimental data. In particular, two features of the mismatch strain in the devices have strong effects on the calculated electronic and transport properties. First, the average effect of the strain is to separate the resonant energy peaks associated with the individual valence subbands in the material. In larger devices, the strain is less relaxed by the free surfaces, so the HH–LH subband energy separation is larger. Second, strain nonuniformity in the devices is responsible for fine structure in the resonant tunneling current peaks. This effect is the source of low-energy ring-like states that are found in the small cylindrical quantum dots, and the edge states found in quantum wires over a range of sizes.

The main weaknesses in the method are in the simplified quantum mechanical model. The real-space calculation is based on a k-space material model that is accurate near $k=0$. The resonant tunneling model assumes ballistic transport of a single charge carrier, and contact is made with experiments in only an approximate way. A linear elastic constitutive model provides a good approximation for the strain, although the approach has limitations for such small, highly strained structures.[29] Finally, the strain effect is treated as a linear perturbation to a perfect crystal Hamiltonian, so the fully coupled nature of strain and electronic properties through the chemical bonding is not considered. However, the technique shown here is a promising, computationally inexpensive way to determine strain effects on electronic properties in semiconductors. The means to overcome the noted shortcomings are under development.

ACKNOWLEDGMENTS

One of the authors (H.T.J.) would like to acknowledge helpful discussions with V. B. Shenoy and R. Phillips regarding the application of the finite element method to quantum mechanics. The authors are also grateful for the cooperation of J. Caro in providing access to experimental data. The research support of the Office of Naval Research, Contract No. N00014-95-1-0239, and the MRSEC Program of the National Science Foundation, under Award No. DMR-9632524, is gratefully acknowledged (H.T.J. and L.B.F.). This work has also been supported in part by an NSF Career Award (DMR-9702725), the ONR Young Investigator Program (N00014-95-1-0729), and a Sloan Foundation Fellowship (C.D.A. and A.Z.).

APPENDIX A

The strain-induced potential $V_{\epsilon}^{\alpha\beta}(\mathbf{r})$ is given by

$$V_{\epsilon}^{\alpha\beta}(\mathbf{r}) = \begin{array}{c} \\ \left|\frac{3}{2},+\frac{3}{2}\right\rangle \\ \left|\frac{3}{2},-\frac{3}{2}\right\rangle \\ \left|\frac{3}{2},+\frac{1}{2}\right\rangle \\ \left|\frac{3}{2},-\frac{1}{2}\right\rangle \end{array} \begin{array}{c} \begin{array}{cccc} \left|\frac{3}{2},+\frac{3}{2}\right\rangle & \left|\frac{3}{2},-\frac{3}{2}\right\rangle & \left|\frac{3}{2},+\frac{1}{2}\right\rangle & \left|\frac{3}{2},-\frac{1}{2}\right\rangle \end{array} \\ \begin{pmatrix} D_{ij}^{11}(\mathbf{r})\epsilon_{ij}(\mathbf{r}) & D_{ij}^{12}(\mathbf{r})\epsilon_{ij}(\mathbf{r}) & D_{ij}^{13}(\mathbf{r})\epsilon_{ij}(\mathbf{r}) & D_{ij}^{14}(\mathbf{r})\epsilon_{ij}(\mathbf{r}) \\ D_{ij}^{21}(\mathbf{r})\epsilon_{ij}(\mathbf{r}) & D_{ij}^{22}(\mathbf{r})\epsilon_{ij}(\mathbf{r}) & D_{ij}^{23}(\mathbf{r})\epsilon_{ij}(\mathbf{r}) & D_{ij}^{24}(\mathbf{r})\epsilon_{ij}(\mathbf{r}) \\ D_{ij}^{31}(\mathbf{r})\epsilon_{ij}(\mathbf{r}) & D_{ij}^{32}(\mathbf{r})\epsilon_{ij}(\mathbf{r}) & D_{ij}^{33}(\mathbf{r})\epsilon_{ij}(\mathbf{r}) & D_{ij}^{34}(\mathbf{r})\epsilon_{ij}(\mathbf{r}) \\ D_{ij}^{41}(\mathbf{r})\epsilon_{ij}(\mathbf{r}) & D_{ij}^{42}(\mathbf{r})\epsilon_{ij}(\mathbf{r}) & D_{ij}^{43}(\mathbf{r})\epsilon_{ij}(\mathbf{r}) & D_{ij}^{44}(\mathbf{r})\epsilon_{ij}(\mathbf{r}) \end{pmatrix} \end{array}, \tag{A1}$$

where each component $D_{ij}^{\alpha\beta}(\mathbf{r})$ of the matrix for fixed $\alpha\beta$ forms a scalar product with the strain tensor $\epsilon_{ij}(\mathbf{r})$ through summation over i and j. And similarly, the $\mathbf{k}\cdot\mathbf{p}$ Hamiltonian given by Luttinger and Kohn takes the form

$$H_{k\cdot p}^{\alpha\beta}(\mathbf{r}) = \begin{array}{c} \\ \left|\frac{3}{2},+\frac{3}{2}\right\rangle \\ \left|\frac{3}{2},-\frac{3}{2}\right\rangle \\ \left|\frac{3}{2},+\frac{1}{2}\right\rangle \\ \left|\frac{3}{2},-\frac{1}{2}\right\rangle \end{array} \begin{array}{c} \begin{array}{cccc} \left|\frac{3}{2},+\frac{3}{2}\right\rangle & \left|\frac{3}{2},-\frac{3}{2}\right\rangle & \left|\frac{3}{2},+\frac{1}{2}\right\rangle & \left|\frac{3}{2},-\frac{1}{2}\right\rangle \end{array} \\ \begin{pmatrix} L_{ij}^{11}(\mathbf{r})\nabla_{ij}^2 & L_{ij}^{12}(\mathbf{r})\nabla_{ij}^2 & L_{ij}^{13}(\mathbf{r})\nabla_{ij}^2 & L_{ij}^{14}(\mathbf{r})\nabla_{ij}^2 \\ L_{ij}^{21}(\mathbf{r})\nabla_{ij}^2 & L_{ij}^{22}(\mathbf{r})\nabla_{ij}^2 & L_{ij}^{23}(\mathbf{r})\nabla_{ij}^2 & L_{ij}^{24}(\mathbf{r})\nabla_{ij}^2 \\ L_{ij}^{31}(\mathbf{r})\nabla_{ij}^2 & L_{ij}^{32}(\mathbf{r})\nabla_{ij}^2 & L_{ij}^{33}(\mathbf{r})\nabla_{ij}^2 & L_{ij}^{34}(\mathbf{r})\nabla_{ij}^2 \\ L_{ij}^{41}(\mathbf{r})\nabla_{ij}^2 & L_{ij}^{42}(\mathbf{r})\nabla_{ij}^2 & L_{ij}^{43}(\mathbf{r})\nabla_{ij}^2 & L_{ij}^{44}(\mathbf{r})\nabla_{ij}^2 \end{pmatrix} \end{array}, \tag{A2}$$

where the each of the matrix components $L_{ij}^{\alpha\beta}(\mathbf{r})$ for fixed $\alpha\beta$ form a scalar product with the operator ∇_{ij}^2. The components $D_{ij}^{\alpha\beta}(\mathbf{r})$ and $L_{ij}^{\alpha\beta}(\mathbf{r})$ have very similar form. The deformation potential components $D_{ij}^{\alpha\beta}(\mathbf{r})$ are

$$D_{ij}^{11}(\mathbf{r}) = D_{ij}^{22}(\mathbf{r}) = \begin{bmatrix} a+b/2 & 0 & 0 \\ 0 & a+b/2 & 0 \\ 0 & 0 & a-b \end{bmatrix},$$

$$D_{ij}^{33}(\mathbf{r}) = D_{ij}^{44}(\mathbf{r}) = \begin{bmatrix} a-b/2 & 0 & 0 \\ 0 & a-b/2 & 0 \\ 0 & 0 & a+b \end{bmatrix},$$

$$D_{ij}^{13}(\mathbf{r}) = D_{ij}^{31*}(\mathbf{r}) = -D_{ij}^{24*}(\mathbf{r}) = -D_{ij}^{42}(\mathbf{r}) = \begin{bmatrix} 0 & 0 & -id/2 \\ 0 & 0 & -d/2 \\ -id/2 & -d/2 & 0 \end{bmatrix}, \tag{A3}$$

$$D_{ij}^{14}(\mathbf{r}) = D_{ij}^{23*}(\mathbf{r}) = D_{ij}^{32}(\mathbf{r}) = D_{ij}^{41*}(\mathbf{r}) = \begin{bmatrix} \frac{\sqrt{3}}{2}b & -id/2 & 0 \\ -id/2 & -\frac{\sqrt{3}}{2}b & 0 \\ 0 & 0 & 0 \end{bmatrix},$$

$$D_{ij}^{12}(\mathbf{r}) = D_{ij}^{21}(\mathbf{r}) = D_{ij}^{34}(\mathbf{r}) = D_{ij}^{43}(\mathbf{r}) = \begin{bmatrix} 0 & 0 & 0 \\ 0 & 0 & 0 \\ 0 & 0 & 0 \end{bmatrix}.$$

The Hamiltonian components $L_{ij}^{\alpha\beta}(\mathbf{r})$ can be obtained by making the substitutions $(\hbar^2/2m_0)\gamma_1 \leftrightarrow a$, $(\hbar^2/m_0)\gamma_2 \leftrightarrow b$, and $(\sqrt{3}\hbar^2/m_0)\gamma_3 \leftrightarrow d$ into the expressions for the components $D_{ij}^{\alpha\beta}(\mathbf{r})$, where γ_1, γ_2, and γ_3 are the Luttinger–Kohn parameters. Values for the deformation potential constants and the Luttinger–Kohn parameters for Si and Ge are given below. Values for alloys of Si and Ge are interpolated from values for the bulk materials.

	a (eV)	b (eV)	d (eV)	γ_1	γ_2	γ_3
Si	2.1	−1.5	−3.4	4.29	0.34	1.45
Ge	2.0	−2.2	−4.4	13.4	4.24	5.59

APPENDIX B

To obtain the finite element form of the Schrödinger equation, the physical region is divided into elements, which are taken here to be four-noded quadrilaterals for the two-dimensional quantum wire and eight-noded bricks for the three-dimensional quantum dot. The wave-function Ψ^{α}, wave-function gradient $\nabla\Psi^{\alpha}$, and potential $V^{\alpha\beta}$ are expressed in terms of discretized values at the nodes, and values within the elements are determined by linear interpolation using linear shape functions $N(\mathbf{r})$. A group of quadrilateral elements and the linear shape function for an associated node are shown in Fig. 14.

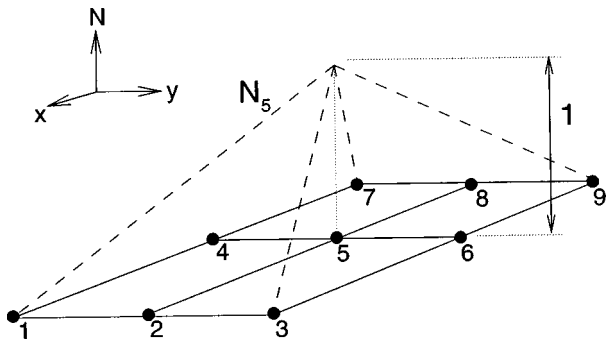

FIG. 14. Elements, nodes, and a representative shape function in the two-dimensional finite element formulation.

The form of the Schrödinger equation to be solved is

$$L^{\alpha\beta}(\mathbf{r})\nabla^2\Psi^{\beta}(\mathbf{r})+V^{\alpha\beta}(\mathbf{r})\Psi^{\beta}(\mathbf{r})=E\Psi^{\alpha}(\mathbf{r}). \tag{B1}$$

The weak form of the equation is obtained by multiplying by $\Psi(\mathbf{r})$ and integrating over the volume of the body. The first term is integrated by parts, and the functional corresponding to the weak form is given by

$$\Pi(\Psi^{\alpha})=\int_R \nabla\Psi^{\alpha}L^{\alpha\beta}\nabla\Psi^{\beta}dR + \int_R \Psi^{\alpha}V^{\alpha\beta}\Psi^{\beta}dR-E\int_R \Psi^{\alpha}\Psi^{\beta}dR. \tag{B2}$$

The spatially varying fields are then discretized using the shape functions $N(\mathbf{r})$ to get

$$\Pi(\Psi_A^{\alpha})=\sum_A\sum_B\left[\int_R \Psi_A^{\alpha}\nabla N_A L^{\alpha\beta}\Psi_B^{\beta}\nabla N_B dR + \int_R \Psi_A^{\alpha}N_A\sum_C V_C^{\alpha\beta}N_C\Psi_B^{\beta}N_B dR - E\int_R \Psi_A^{\alpha}\Psi_B^{\beta}N_A N_B\right]dR. \tag{B3}$$

The total variation of the functional $\Pi(\Psi_A^{\alpha})$ is then minimized with respect to the nodal values of the wave-function Ψ_B^{β} so that

$$\frac{d\Pi(\Psi_A^{\alpha})}{d\Psi_B^{\beta}}=0, \tag{B4}$$

thus

$$\Psi_A^{\alpha}\sum_A\sum_B\left[\int_R \nabla N_A L^{\alpha\beta}\nabla N_B dR+\int_R N_A\sum_C V_C^{\alpha\beta}N_C N_B dR - E\int_R N_A N_B dR\right]=0. \tag{B5}$$

Replacing integrals over the region R with integration over individual element volumes (Ω^e) and a summation over all elements, the final finite element form of the equation becomes

$$\sum^{\text{elems}}\left[\sum_A\sum_B\int_{\Omega^e}\left(\nabla N_A L^{\alpha\beta}\nabla N_B + N_A N_B\sum_C V_C^{\alpha\beta}N_C\right)d\Omega\right]\Psi_B^{\beta} = E\sum^{\text{elems}}\left[\sum_A\sum_B\int_{\Omega^e}N_A N_B d\Omega\right]\Psi_B^{\alpha}. \tag{B6}$$

The contribution of a single element to the left-hand side of the equation is given by the element stiffness matrix. The integration over the element is done numerically at a set of quadrature points. The construction of an element stiffness matrix for the case of two spatial dimensions and a four subband quantum mechanical basis is as follows:

$$k_{\alpha\beta}^e=\int_{\Omega^e}\left(\nabla N_A L^{\alpha\beta}\nabla N_B + N_A N_B\sum_C V_C^{\alpha\beta}N_C\right)d\Omega = \sum_{l=1}^{int.pts.}[\underbrace{\underbrace{\nabla N_A}_{16\times 8}\underbrace{L^{\alpha\beta}}_{8\times 8}\underbrace{\nabla N_B}_{8\times 16}}_{16\times 16} + \underbrace{\underbrace{N_A}_{16\times 4}\underbrace{\sum^{nodes}\left(V_C^{\alpha\beta}N_C\right)}_{4\times 4}\underbrace{N_B}_{4\times 16}}_{16\times 16}]_l \tag{B7}$$

where the tensors $D_{ij}^{\alpha\beta}$ and $L_{ij}^{\alpha\beta}$ given in Appendix A reduce to 2×2 matrices, and the shape function matrix is given by

$$N_A=\left[\begin{array}{cccc|cccc|cccc|cccc} N_1 & N_2 & N_3 & N_4 & 0 & \dots & \dots & 0 & \dots & \dots & 0 & \dots & \dots & 0 & \dots & \dots \\ 0 & \dots & \dots & 0 & N_1 & N_2 & N_3 & N_4 & 0 & \dots & \dots & 0 & \dots & \dots & 0 & \dots \\ \dots & 0 & \dots & \dots & 0 & \dots & \dots & 0 & N_1 & N_2 & N_3 & N_4 & 0 & \dots & \dots & 0 \\ \dots & \dots & 0 & \dots & \dots & 0 & \dots & \dots & 0 & \dots & \dots & 0 & N_1 & N_2 & N_3 & N_4 \end{array}\right], \tag{B8}$$

and the shape function derivative matrix ∇N_A follows in the same form.

The contribution of a single element to the right-hand side of Eq. (B6) is referred to as the element mass matrix and is constructed in a similar way as $k_{\alpha\beta}^e$. The final finite element matrix form of the Schrödinger equation, given by

$$K_{ij}\Psi_j=EM_{ij}\Psi_j, \tag{B9}$$

is constructed by assembling the element stiffness matrices and element mass matrices into global element and mass matrices, K_{ij} and M_{ij}, for the entire device.

[1] A. Zaslavsky, K. R. Milkove, Y. H. Lee, B. Ferland, and T. O. Sedgewick, Appl. Phys. Lett. **67**, 3921 (1995).
[2] C. D. Akyüz, A. Zaslavsky, L. B. Freund, D. A. Syphers, and T. O. Sedgewick, Appl. Phys. Lett. **72**, 1739 (1998).
[3] P. Gassot, U. Gennser, D. M. Symons, A. Zaslavsky, D. A. Gruztmacher, and J. C. Portal, Physica E (to be published).

[4] P. W. Lukey, J. Caro, T. Zijlstra, E. van der Drift, and S. Radelaar, Phys. Rev. B **57**, 7132 (1998).
[5] C. Pryor, M.-E. Pistol, and L. Samuelson, Phys. Rev. B **56**, 10 404 (1997).
[6] C. Pryor, Phys. Rev. B **57**, 7190 (1998).
[7] C. Pryor, http://xxx.lanl.gov/abs/cond-mat/9801225
[8] A. J. Williamson, A. Zunger, and A. Canning, http://xxx.lanl.gov/abs/cond-mat/9801191
[9] M. Grundmann, O. Stier, and D. Bimberg, Phys. Rev. B **52**, 11 969 (1995).
[10] A. Zunger, MRS Bull. **23**, 15 (1998).
[11] M.-E. Pistol, N. Carlsson, C. Persson, W. Seifert, and L. Samuelson, Appl. Phys. Lett. **67**, 1438 (1995).
[12] T. J. Gosling and L. B. Freund, Acta Mater. **44**, 1 (1996).
[13] ABAQUS, Version 5.5, Hibbitt, Karlsson & Sorensen, Inc., Pawtucket, RI 02860 (1995).
[14] J. Linderberg, Comput. Phys. Rep. **6**, 209 (1987).
[15] K. Nakamura, A. Shimizu, M. Koshiba, and K. Hayata, IEEE J. Quantum Electron. **25**, 889 (1989).
[16] A. Zhao, S. R. Cvetkovic, and Z. A. Yang, Opt. Quantum Electron. **25**, 845 (1993).
[17] T. L. Li and K. J. Kuhn, J. Comput. Phys. **115**, 288 (1994).
[18] Chen, Comput. Math. Appl. **31**, 17 (1996).
[19] K. Kujima, K. Mitsunaga, and K. Kyuma, Appl. Phys. Lett. **55**, 882 (1989).
[20] D. J. Kirkner, C. S. Lent, and S. Sivaprakasm, Int. J. Numer. Methods Eng. **29**, 1527 (1990).
[21] Z. Wu and P. P. Ruden, J. Appl. Phys. **74**, 6234 (1993).
[22] Y. Wang, J. Wang, and H. Guo, Phys. Rev. B **49**, 1928 (1994).
[23] T. Inoshita and H. Sakaki, J. Appl. Phys. **79**, 269 (1996).
[24] J. C. Yi and N. Dagli, IEEE J. Quantum Electron. **31**, 208 (1995).
[25] T. Inoshita and H. Sakaki, J. Appl. Phys. **79**, 269 (1996).
[26] E. Tsuchida and M. Tsukada, Phys. Rev. B **52**, 5573 (1995).
[27] G. Strang and G. J. Fix, *An Analysis of the Finite Element Method* (Prentice-Hall, Englewood Cliffs, NJ, 1973), pp. 8 and 41.
[28] J. Singh, *Physics of Semiconductors and Their Heterostructures* (McGraw-Hill, New York, 1993), p. 228.
[29] C. Pryor, J. Kim, L. W. Wang, A. Williamson, and A. Zunger, J. Appl. Phys. **83**, 5 (1998).